A Hybrid Variable-Stiffness Soft Back Support Device

Rohan Khatavkar, The Bach Nguyen, Yuanhao Chen, Hyunglae Lee, *Member, IEEE*, and Jiefeng Sun, *Member, IEEE*

***Abstract*—Back support devices(BSDs) have the potential to mitigate overexertion in industrial tasks and also to provide assistance to people with weak back muscle strength in daily activity. While state-of-the-art active BSDs can offer a high assistive force, they are bulky and heavy, making them uncomfortable for daily use. On the contrary, passive BSDs are compact but need manual adjustment to be versatile. This work presents a hybrid soft BSD that can provide task-oriented assistance by tuning the stiffness (0.58 N/mm, 0.92 N/mm, and 1.7 N/mm) and slack length (0 mm to 67 mm) in a compact design. The tunable stiffness allows for selecting a task-specific force profile, and the slack tuning will ensure that the device enables unhindered movement when assistance is not required. Compared with rigid devices, the device's compliance can potentially increase human comfort. We propose an analytical model that facilitates device design and estimates the device performance. Furthermore, the device's tuning capabilities are evaluated in human squatting and stooping experiments, showing that the desired force profile is correctly applied.**

***Index Terms*—Soft robot applications, prosthetics and exoskeletons, wearable robotics.**

I. Introduction

BACK injuries are among the most prevalent injuries [1], and the medical cost related to back injuries in the US was more than $365 billion in the year 2019 [2]. Back support devices (BSDs) have the potential to mitigate overexertion, which is a cause of the majority of back injuries [3]. Besides overexertion, BSDs could also compensate for reduced trunk muscle strength in the elderly population to assist in daily life activities [4]. BSDs can be classified according to actuation and rigidity, and each category has its advantages and disadvantages.

Active BSDs typically apply a force between the back and the hip using a linkage at the hip joint driven by a motor or series elastic actuator [5]. Though these devices reduce back muscle effort, they are heavy and bulky due to the high torque motor actuation required to support the trunk. Active BSDs driven by artificial muscles have also been reported, e.g., Tsuneyasu et al. developed an active BSD with McKibben-type pneumatic artificial muscles [6] and another active BSD using hydraulic filament artificial muscle was developed by Zhu et al. [7]. Both devices led to reduced back extensor effort. However, they are both tethered devices driven by heavy off-board actuators. Even untethered systems driven by pneumatic artificial muscles, like the Innophys Muscle Suit [8], become bulky due to onboard pneumatic systems.

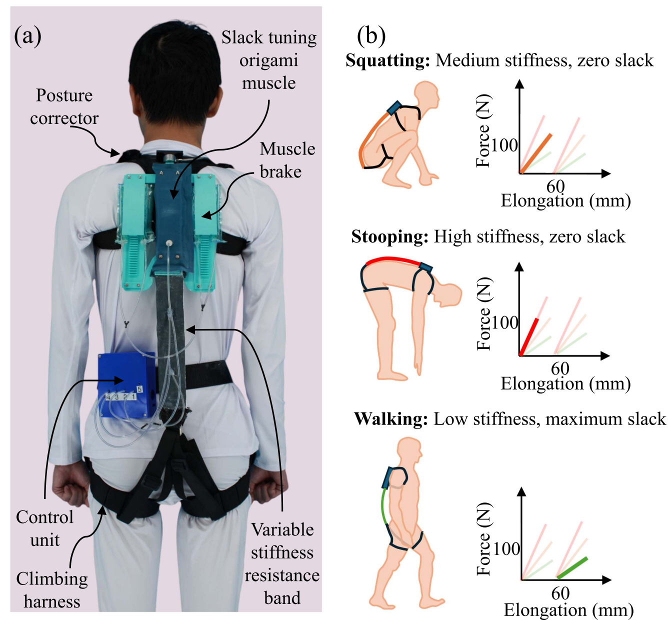

Fig. 1. Overview of our hybrid BSD: (a) A user wearing our hybrid BSD. (b) Task-oriented stiffness and slack tuning capability. A video showing our device is attached as supplementary media and can also be found online: https://youtu.be/e1795O9zEiU.

The passive BSDs generate force through a passive elastic element, thus becoming more compact. Several passive BSDs have shown efficacy in reducing human muscular effort during trunk extension [9], [10]. However, passive BSDs are not tunable and are typically optimized for a single task like squatting. In addition, discomfort and movement restriction may happen due to a mismatch between the device forces and the task demands [11], [12]. A few commercially available passive back exoskeletons, such as Laevo FLEX [13], provide multiple passive elastic

Received 29 September 2024; accepted 1 February 2025. Date of publication 11 February 2025; date of current version 24 February 2025. This article was recommended for publication by Associate Editor Tom Verstraten and Editor Jee-Hwan Ryu upon evaluation of the reviewers' comments. This work was supported by Ira A. Fulton Schools of Engineering, Arizona State University. *(Corresponding author: Jiefeng Sun.)*

This work involved human subjects or animals in its research. Approval of all ethical and experimental procedures and protocols was granted by the Institute Review Board at Arizona State University under Application No. STUDY0020698.

The authors are with the School for Engineering of Matter, Transport and Energy, Arizona State University, Tempe, AZ 85281 USA (e-mail: jiefeng.sun@asu.edu).

This article has supplementary downloadable material available at https://doi.org/10.1109/LRA.2025.3541459, provided by the authors.
Digital Object Identifier 10.1109/LRA.2025.3541459

TABLE I
COMPARISON OF EXISTING UNTETHERED BSDS

Device	Type	Force Generation	Weight	Force Tuning	Slack Tuning
Cray X [5]	Active Rigid	Electric motors	7 kg	Continuous	Continuous
Laevo V2 [9]	Passive Rigid	Compliant mechanism	4 kg	None	None
IX BackX Air [10]	Passive Rigid	Compliant mechanism	3 kg	None	None
Chung et al. [14]	Active Soft	Bowden cable	2.7 kg	Continuous	Continuous
Lamers et al. [15]	Passive soft	Elastic band	1.5 kg	None	None
Muscle Suit [8]	Hybrid Soft	McKibben Type PAM	3.8 kg	Continuous	None
This Device	Hybrid Soft	Variable-stiffness resistance band	1.2 kg	Discrete	Continuous

Note:'Force Generation' indicates the device element applying assistive force, e.g., a variable stiffness resistance band.

elements with varying stiffness values. However, users have to manually replace the passive elastic element every time, which is tedious.

Further, the state-of-the-art BSDs can also be classified as rigid and soft devices. A few devices consisting majorly of soft elements [15], [16], [17] could, in general, be more comfortable than rigid devices for daily use with body attachments optimized for comfort [18], [19], [20], [21]. However, most state-of-the-art soft BSDs are passive as soft actuation technology often cannot provide enough force when untethered [22]. Additionally, emerging soft stiffness tuning technology is unexplored for back support applications due to large stiffness change requirement [23].

In this work, we present a hybrid soft BSD that provides assistance similar to a passive device but can change force profiles without manually replacing any component (Fig. 1(a)). The word "hybrid" indicates that our device offers a balance between the tuning capabilities of active devices and the compactness and lightweight of passive devices as indicated in Table I. Additionally, due to its softness, it is can be more comfortable to wear in daily activities. The proposed device integrates a variable-stiffness (VS) resistance band and a slack-tuning mechanism that can apply a desired predefined force profile (stiffness and slack) for various tasks. For example, as shown in Fig. 1(b), the device can be switched to a higher stiffness mode for stooping and a lower stiffness mode for squatting [24]. With slack tuning, the device also allows unhindered walking with a tuned slack length. Our novel integration of soft components addressed the challenges of achieving a high blocking force with a wide slack tuning range in a compact and lightweight design, as well as reliable stiffness control across a discrete range.

The major contributions of this work are as follows: (1) We presented a novel BSD design that allows users to choose between predefined back support force profiles by integrating variable-stiffness and slack-tuning elements. (2) We present an analytical model to estimate the device performance and facilitate device design, e.g., design a required stiffness for a desired force profile. (3) We validate the tuning capabilities of our device with simulated activities of daily living (squatting and stooping).

II. DEVICE DESIGN

This section gives an overview of the device design and explains how stiffness and slack tuning are achieved.

A. Device Overview

The device consists of three main parts: a VS resistance band, a slack-tuning origami muscle, and muscle brakes, as shown in Fig. 2(a). The VS resistance band is the elastic element applying the assistive trunk extension torque. It is connected in series with the origami muscle that is responsible for tuning the slack. The upper end of the origami muscle is secured to the user's upper back using a posture corrector (Hallway Stories), while the lower end of the VS resistance band is connected to the thigh straps of a climbing harness (TCH-107-2139-ES-S-XL-BLK-ORG, Fusion) using inextensible fabric straps. The device will apply a tensile force between the thighs and the upper back as the trunk undergoes flexion, resulting in a moment around the hip joint that assists trunk extension. The force provided by the device over the range of motion can be tuned by changing the stiffness of the VS resistance band using layer jamming. The slack can be reduced by contracting the origami muscle. Slack tuning allows the user to define a critical trunk flexion angle beyond which the device begins applying a force. We intentionally designed the origami muscle to be small and included two muscle brakes in parallel with the origami muscle to hold it in the contracted state. Such a combination resolves the challenge that a bulky artificial muscle needs to be used to block a significantly large force, ensuring a compact and lightweight device (refer to Table I).

B. VS Resistance Band

1) Design: The VS resistance band's stiffness is tuned by stiffening discrete segments of an elastic band (50-125 lbs pull-up band, LEEKEY) with teethed layer jamming structures (Patch 1 and Patch 2), as shown in Fig. 2(b). We selected teethed layer jamming [25], [26] because it can withstand the high force required by BSDs while being compliant in a compact size [27]. A patch consists of two flexible teethed layers (referred to as patch layers) incorporated inside an elastic enclosure (azurelife), and the teeth engage when the elastic enclosure is vacuumed due to the patch layers bending elastically at the flexural hinges. The patch layers spring back with assistance from retaining foam inserts when the vacuum pressure is released.

The VS resistance band includes two jamming patches and is designed to operate in three stiffness levels (No patch jammed, patch 1 jammed, and both patches 1 and 2 jammed). The patch layers are located inside rectangular cutouts in the elastic band, allowing the patch to have low stiffness when unjammed and significantly increase in stiffness when jammed. Further, the two

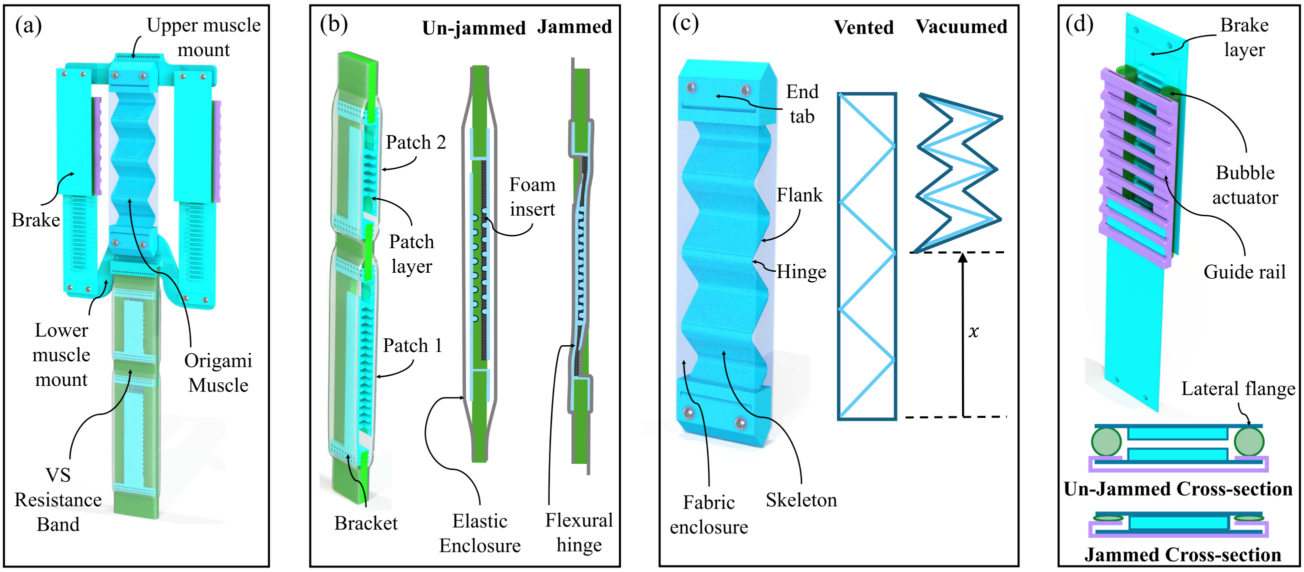

Fig. 2. System Design. (a) Device assembly. (b) VS resistance band's cross-sectional view and the working principle of the teethed layer jamming structures (Patch 1 and Patch 2) inside cutouts. (c) 3D model and the contraction principle of the vacuum-driven origami muscle consisting of a zig-zag skeleton inside an airtight enclosure. (d) 3D model and the working principle of the muscle brake.

patches have different lengths, chosen specifically to achieve the desired stiffness levels according to the modeling in Section III. The longer patch (patch 1) consists of two 97 $\times$ 21 $\times$ 0.65 mm (length $\times$ width $\times$ thickness) patch layers with 17 teeth each, and the shorter patch (patch 2) has two 50 $\times$ 21 $\times$ 0.65 mm patch layers with 6 teeth each. The teeth are 2 mm wide and 3 mm high with a backlash of 0.4 mm. The 0.65 mm thick patch layers are highly compliant and thus capable of following the VS resistance band curvature during operation.

2) Fabrication: To fabricate the VS resistance band, two cutouts of 21 $\times$ 54 mm and 21 $\times$ 100.4 mm are cut into an elastic band. The patch layers are 3D printed (MK-4, Prusa Research) with poly-lactic acid (PLA). The patch layers have a bracket that slides onto the elastic band, and this bracket is sewn to the band. One patch layer is sewn to one shorter edge of the cutout, and the other patch layer is sewn to the other shorter edge, as shown in Fig. 2(b). Polyurethane foam inserts (#8614K81, McMaster-Carr) were adhered in the space between adjacent teeth to facilitate disengagement when the patch is vented. Finally, the elastic enclosure is wrapped around and adhered to form two separate patches using a polyurethane-based adhesive (Marine Glue, 3M). The upper end of the VS resistance band is then sewn to a 3D-printed lower muscle mount.

C. Origami Muscle

1) Design: We selected a vacuum-driven origami muscle for slack tuning due to its high contraction ratio that enables a wide slack range [28]. The origami muscle consisting of a zig-zag skeleton inside a fabric enclosure, as shown in Fig. 2(c), contracts when the fabric enclosure collapses on vacuuming, folding the skeleton at its hinges. When the vacuum in the fabric enclosure is released, the origami muscle returns to its rest length as the skeleton springs back.

2) Fabrication: The zig-zag skeleton is 40 mm wide, 0.4 mm thick at the hinges, 1 mm thick at the flanks, and the skeleton's 4 mm long hinges are 90° at its rest length. The skeleton was 3D printed in the unfolded state with PLA (MK4, Prusa Research) and then folded at the hinges to obtain the zig-zag shape. The flanks at the ends of the skeleton were inserted and adhered into slots in the end tabs. The fabric enclosure was fabricated by heat-sealing polyurethane-coated nylon fabric, with the skeleton inserted inside. Finally, the fabric enclosure and the skeleton were connected to the lower muscle mount.

D. Muscle Brakes

1) Design: We selected a teethed layer jamming structure similar to that in the VS resistance band to design the muscle brakes due to its high force-withstanding capacity. The disengagement and engagement of flexible teethed layers (referred to as brake layers) are controlled by bubble actuators, which are soft actuators that use an enclosed air chamber to radially expand on inflation and collapse on vacuuming. The bubble actuators are placed between the two brake layers as shown in Fig. 2(d), and they disengage the muscle brake when inflated and engage the muscle brake when vacuumed.

The brake layers have lateral flanges beside the teethed region (Fig. 2(d)). Bubble actuators are positioned between the lateral flanges and a guide rail in which the other brake layer slides. Each muscle brake consists of two brake layers with 23 teeth each. The teeth are 15 $\times$ 2 $\times$ 4 mm (wide, thick, high). A minimum of six brake layer teeth are engaged when the origami muscle is at rest length. The brake layers are 0.65 mm thick and 39 mm wide. The bubble actuators are 10 mm in diameter when inflated and 110 mm long. The muscle brake assembly is 210 mm in length and is longer than the origami muscle to ensure that the stroke of the origami muscle is equal to that of the muscle brakes.

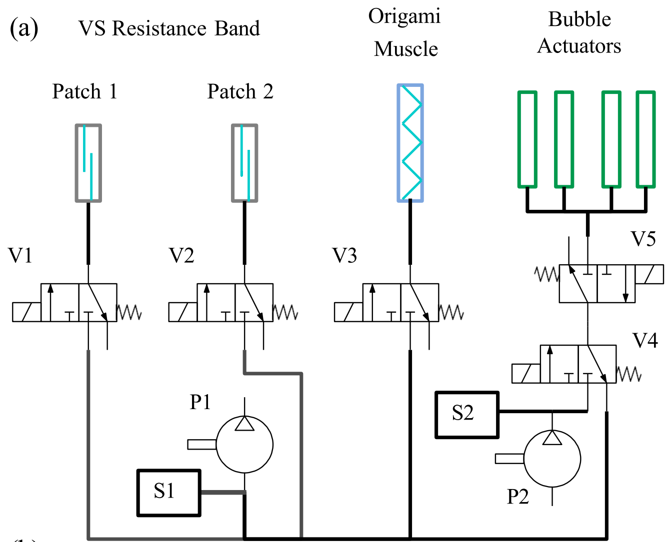

(b)

Device Action	P1	P2	V1	V2	V3	V4	V5
No jamming	1	0	0	0	0	0	1
Jamming Patch 1	1	0	1	0	0	0	1
Jamming Patch 1 and 2	1	0	1	1	0	0	1
Bubble actuator inflation	0	1	0	0	0	1	1
Bubble actuator vacuuming	1	0	0	0	0	0	1
Origami muscle contraction	1	0	0	0	1	1	0
Origami muscle extension	0	0	0	0	0	0	0

Fig. 3. (a) Pneumatic system schematic. (b) Truth table depicting the pneumatic control logic.

2) Fabrication: The brake layers were 3D printed (MK-4, Prusa Research) with PLA. A heat-sealable bagging film (1678, Fiber Glast) was used to fabricate the bubble actuators by heat-sealing. The bubble actuator then adhered to the lateral flange of a brake layer. Finally, the guide rail was adhered to the bubble.

E. Pneumatic and Electronic Systems

The back support device is operated using a portable pneumatic system shown in Fig. 3(a). It consists of two air pumps, P1 (vacuuming) and P2 (positive pressure) (2000 series, Dynaflo, 62 dB), five 3 port 2-way valves V1-V5 (X-valve, Parker), and two differential pressure sensors, S1 and S2 (SSCDRRN015PDAA5, Honeywell). The air pump and the valve weigh only 23 g and 4.5 g, respectively, with small form factors that facilitate the integration of the pneumatic system in an untethered control unit weighing 300 g.

The truth table for device actions is shown in Fig. 3(b). The muscle brakes are engaged while operating the device to maintain constant slack by vacuuming the bubble actuators using P1 with V4 closed and V5 open. V1 and V2 are opened in addition to V5 to operate the device in the higher stiffness modes corresponding to one of the VS resistance band patches being jammed or both the patches being jammed, respectively. The bubble actuators are inflated by P2 with V4 and V5 opened before contracting the origami muscle using P1 by opening V3. The bubble actuators are similarly inflated before extending the origami muscle. The pressure generated by the pumps P1 and P2, respectively, are measured by the pressure sensors S1 and S2, respectively.

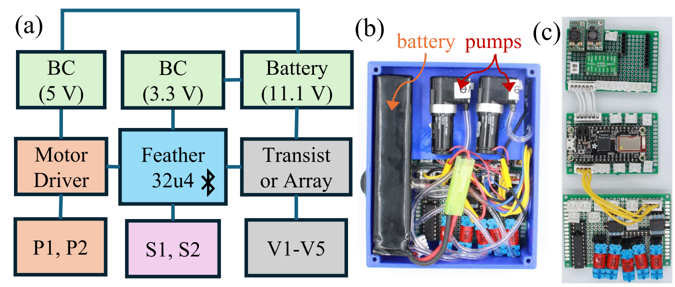

Fig. 4. (a) Schematic of the electronic system. (b) Image of the open control unit. (c) Individual circuit boards within the control unit.

The electronic circuit that controls the pneumatic system is illustrated in Fig. 4. An onboard microcontroller (Feather 32u4, Adafruit) operates the pumps and valves based on serial input from a remote device via Bluetooth. The microcontroller controls the pumps through a motor driver (TB6612FNG) and switches the valves through a transistor array (TBD62083APG-ND). A 2000 mAh, 11.1 V Lithium Polymer (LiPo) battery powers the portable circuit and can sustain operation for up to 705 mode switches in a day. The LiPo battery powers the valves directly, the microcontroller through a 3.3 V buck converter, and the pumps through a 5 V buck converter.

III. Modeling of the Device

This section presents analytical models of the VS resistance band and the origami muscle as parts of the whole device model to facilitate the design of the desired stiffness levels and the desired slack range.

A. Model of the vs Resistance Band

The VS resistance band is modeled using an equivalent spring network in Fig. 5(a). The stiffness of the patches k_{p1} and k_{p2} change based on whether they are jammed or not

$$k_{\mathrm{p}i} = \begin{cases} \bar{k}_{\mathrm{p}i} & \text{if patch } i \text{ is jammed,} \\ 0 & \text{if patch } i \text{ is unjammed,} \end{cases} \tag{1}$$

with $i = 1$ or 2 representing patch 1 or 2. Note that $k_{\mathrm{p}i}$ is a variable while $\bar{k}_{\mathrm{p}i}$ is a parameter measured experimentally.

The VS resistance band's stiffness k_{rb} is a function of $k_{\mathrm{p}i}$

$$k_{\mathrm{rb}}(k_{\mathrm{p}i}) = \frac{1}{\left(\frac{1}{k_{\mathrm{b}}} + \frac{1}{2k_{\mathrm{s1}}+k_{\mathrm{p1}}} + \frac{1}{k_{\mathrm{m}}} + \frac{1}{2k_{\mathrm{s2}}+k_{\mathrm{p2}}} + \frac{1}{k_{\mathrm{t}}}\right)} + k_{\mathrm{enc}}, \tag{2}$$

where k_{b}, k_{m} and k_{t} are the stiffness of the bottom, middle, and top regions of the VS resistance band, k_{s1} and k_{s2} are the stiffness of the VS resistance band regions beside the cutouts, and k_{enc} is the stiffness of the elastic enclosure determined via tensile testing.

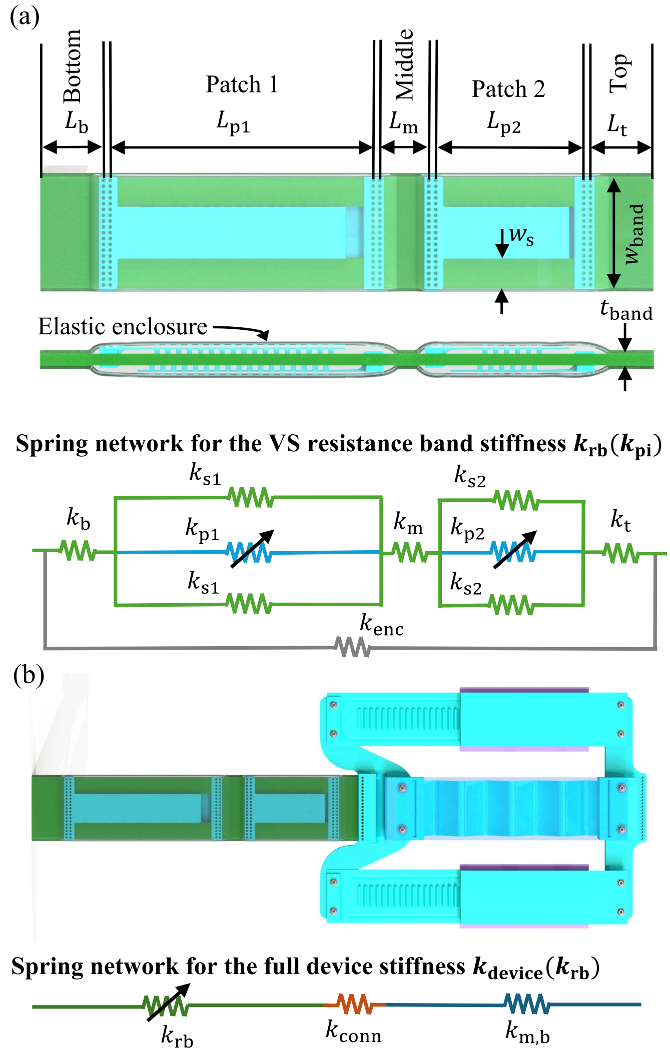

Fig. 5. (a) Dimensions of the elastic band with cutouts and the spring network for modeling the VS resistance band. (b) Spring network equivalent to the full device stiffness.

k_b, k_m, k_t, k_{s1} and k_{s2} are estimated using the formula $w_{band} t_{band} E_{band}/L_{band}$, where L_{band} w_{band}, t_{band} are the length, width, and thickness of the corresponding regions, and E_{band} is the young's modulus of the elastic band (determined via tensile testing).

B. Model of the Origami Muscle

We modeled the origami muscle to estimate its peak blocked force and the maximum contraction. Estimation of the peak blocked force is necessary to ensure the designed contracted origami muscle can block the weight of the device. Estimation of the maximum contraction is required to achieve the desired slack range.

In Fig. 6, the origami muscle is simplified to two dimensions and only its cross-section is shown. The zig-zag skeleton's hinges are modeled as torsional springs. We assume the fabric enclosure deforms into a parabolic arc under vacuum pressure, and the fabric is in-stretchable. Considering the force balance of a skeleton flank adjacent to the end tab, blocked force $F_b(\theta)$ can be calculated through the balance of the contraction force from the fabric due to the vacuum pressure F_v and the retaining force applied by the skeleton F_r due to hinge elasticity [28]:

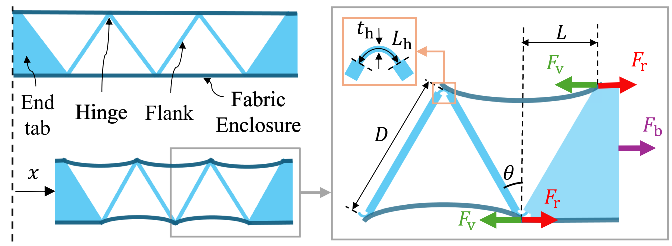

Fig. 6. Schematic showing the origami muscle modeling under vacuum.

$$F_b(\theta) = 2\left(F_v(\theta) - F_r(\theta)\right), \tag{3}$$

where θ is half of the opening angle of the skeleton. They all change with respect to θ. F_r is given by

$$F_r(\theta) = K_h(\theta_0 - \theta)/(D\cos\theta), \tag{4}$$

where the torsional stiffness of the skeleton hinge K_h is given by $K_h = E_s W t_h^3/6L_h$ with E_s and W being the skeleton's Young's modulus and width, and t_h and L_h being the hinge thickness and arc length (equal to the planar hinge length before folding the skeleton); $\theta = \theta_0$ at rest length of the origami muscle; and D is the skeleton flank's length. Further, F_v is given by

$$F_v(\theta) = -\frac{\Delta P W}{2}\left(\frac{D(\cos^2\theta - \sin^2\theta)}{\cos\theta} - \frac{\lambda(\theta)(\mu^{\frac{1}{2}}\cos\theta - \mu^{\frac{1}{2}} D^2 \sin^2\theta\cos\theta)}{\cos\theta}\right), \tag{5}$$

where ΔP is the pressure difference between the atmospheric and vacuum pressures inside the fabric enclosure. λ and μ are given as:

$$\lambda(\theta) = 1 + (\theta_0 - \theta)\left(\frac{D}{L_0} - 1\right)/\theta_0, \tag{6}$$

with $L = L_0$ at the rest length of the origami muscle; and $\mu = L_0^2 - D^2\sin^2\theta$.

Given a blocking force F_b (the weight of our device in this work), we can solve for θ in (3) and calculate the contraction of the origami muscle with respect to θ

$$x(\theta) = 2ND(\sin\theta_0 - \sin\theta), \tag{7}$$

where N is the number of hinges in the skeleton.

C. Model-Based Device Design

To achieve the desired force profile, we need a stiffness model for the full device, as shown in Fig. 5(b). Its stiffness combines the stiffness of VS resistance band k_{rb}, the muscle stiffness $k_{m,b}$, and the stiffness of the connecting elements k_{conn} (e.g., sewing):

$$k_{device}(k_{pi}) = \left(\frac{1}{k_{rb}(k_{pi})} + \frac{1}{k_{m,b}} + \frac{1}{k_{conn}}\right)^{-1}, \tag{8}$$

where $k_{\text{m,b}}$ is determined via tensile testing of the origami muscle assembly, and k_{conn} can be inversely found with a full device force test. The $k_{\text{p}i}$ in the bracket indicates that k_{device} changes based on the jamming states of the patches.

As a starting point for design iteration, we assumed that parameters $k_{\text{m,b}}$, k_{conn}, $\bar{k}_{\text{p1}}$, and $\bar{k}_{\text{p2}}$ are infinitely large and calculated the geometric parameters of the VS resistance band needed to achieve the desired stiffness levels using (2) and (8). Further, the origami muscle is designed to be able to block a force equal to the device's weight at its maximum contraction and (3) was used to determine the minimum possible θ corresponding to the maximum contraction under the device weight for selected feasible skeleton dimensions D, W, θ_0. The obtained minimum value of θ was used to verify if the required contraction can be achieved using (7). If not, we iterated with new skeleton dimensions to achieve the required contraction. Further, the muscle brake was designed to match its stroke with the origami muscle contraction. We fabricated and characterized the individual components and the full device to obtain the experimentally determined design parameters ($k_{\text{m,b}}$, k_{conn}, $\bar{k}_{\text{p1}}$, and $\bar{k}_{\text{p2}}$) and used them to refine the design to achieve the desired device parameters.

A device designed in this way can achieve the desired stiffness values and slack range to apply a hybrid assistive force F_{hybrid} as a function of the variable stiffness $k_{\text{p}i}$, variable slack x, and the angle between the trunk and the hip α, as described by $F_{\text{hybrid}} = f(k_{\text{p}i}, x, \alpha)$. By controlling the value of $k_{\text{p}i}$ and x, we can tune the device's force profile, and thus we have more control over passive devices, where passive assistive force $F_{\text{passive}} = g(\alpha)$, a function of only α, results in a fixed force profile.

IV. Device Characterization

We conducted a series of force tests using a tensile testing machine (#3367, Instron) to characterize the device. We tested the individual components to verify if they could withstand the peak device force and also estimated their stiffness to verify the analytical stiffness model. For the characterization, we selected $w_{\text{t}} = w_{\text{m}} = w_{\text{b}} = 45$ mm, $t_{\text{t}} = t_{\text{m}} = t_{\text{b}} = 4.5$ mm, $L_{\text{t}} = L_{\text{b}} = 25$ mm, $L_{\text{m}} = 20$ mm, $w_{\text{s}} = 12$ mm, $t_{\text{s}} = 4.5$ mm, $L_{\text{p1}} = 54$ mm, $L_{\text{p2}} = 100.4$ mm, $\theta_0 = 90°$, $D = 24$ mm, and $W = 40$ mm.

A. Component Characterization

1) Jamming Patches: To test the shorter patch (patch 2 in Fig. 2(b), we fabricated it in isolation with the patch layers enclosed in a polyethene enclosure being heat-sealed. The enclosure was significantly longer than the total length of the patch layers to ensure that the enclosure was not in tension during the force test. Fig. 7(a) shows the force vs displacement characteristics of the patch at the jammed condition. Its stiffness is measured to be 248.01 N/mm, and it can block a force of more than 290 N, which is greater than the required peak of the VS resistance band (164 N). The stiffness of the longer patch (patch 1) in the jammed state was similarly evaluated to be 282.96 N/mm.

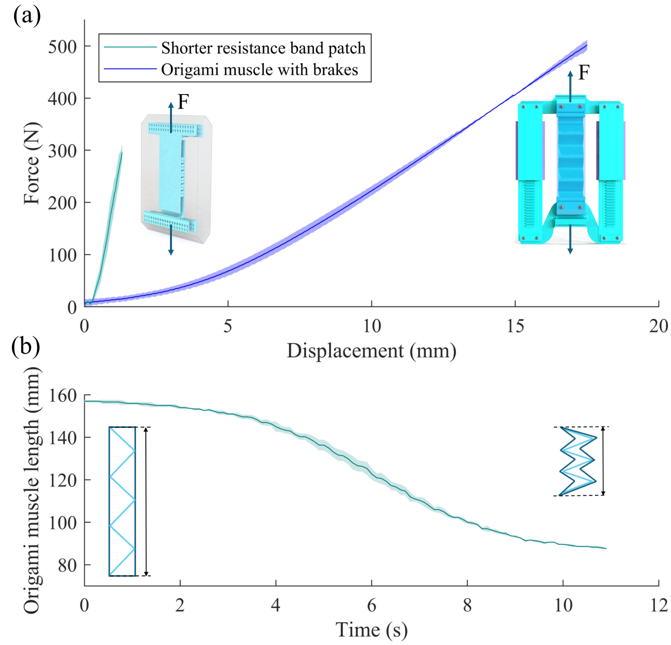

Fig. 7. (a) Tensile testing of the shorter patch and the muscle brakes with origami muscle (only bubble actuators vacuumed, origami muscle at atmospheric pressure). (b) Origami muscle's length changes with respect to time in the actuation test.

2) Origami Muscle: Similar to the jamming patch, we conducted a force test on the origami muscle assembly to evaluate its blocking force. The force test also provided the stiffness of the origami muscle assembly, which is useful in estimating the stiffness of the device. Fig. 7(a) shows that the origami muscle assembly can block a force of 495 N without the muscle brakes slipping, and its stiffness is 24.59 N/mm.

We control the origami muscle contraction using a timing-based open-loop strategy owing to a small variation of its external load (just the weight of the device). Towards this, we measured the origami muscle contraction with respect to time. In the experiment, the origami muscle was vacuumed from its rest length till it reached its maximum contraction. A video of the origami muscle contraction was analysed in Tracker software (Physlets) to measure the contraction with respect to time. The experiments were repeated three times, and no significant variation is observed (standard deviation $\pm 1.61\%$) in Fig. 7(b).

B. Full Device Characterization

To prepare for the testing, as shown in the inset of Fig. 8(b), first, the posture corrector and the climbing harness were removed from the device. The test was conducted for six modes shown in Fig. 8(a). We tested the three stiffness levels in the maximum slack (mode 1-3) and zero slack (mode 4-6) as they result in the lowest and the highest force applied by the device. In the experiment, the upper muscle mount and the bottom of the VS resistance band were stretched by the Instron tensile machine at 1 mm/s. Each tensile test was repeated thrice. We tested the device in two modes: maximum slack and minimum slack. Before testing, the distance between the Instron grippers was set

(a)

Device Mode →	1	2	3	4	5	6
Patch 1	Unjammed	Jammed	Jammed	Unjammed	Jammed	Jammed
Patch 2	Unjammed	Unjammed	Jammed	Unjammed	Unjammed	Jammed
Origami muscle	Max. slack	Max. slack	Max. slack	Min. slack	Min. slack	Min. slack

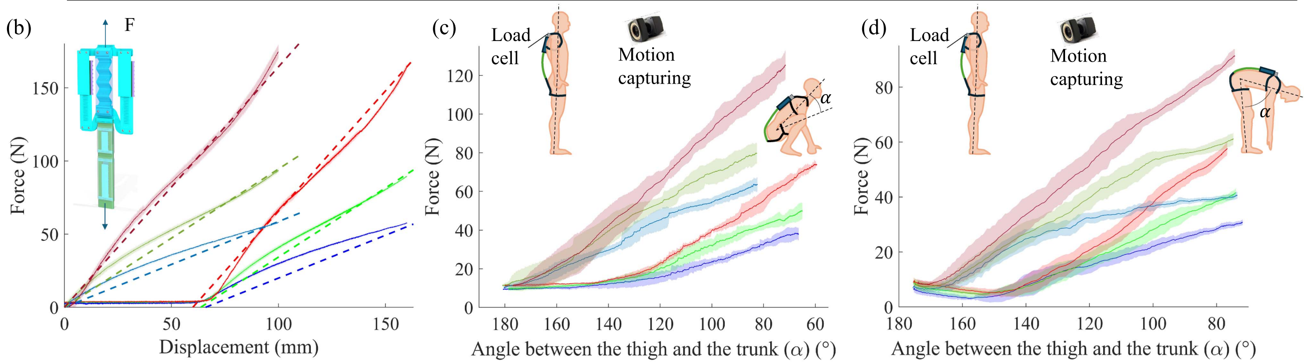

Fig. 8. (a) Device modes. (b) Tensile testing results of the device across its modes. Solid lines with shaded regions indicate the mean and standard deviation of experimental results, and dotted lines indicate analytical curves. (c) Force vs angle between the trunk and the hip characteristics of the device while squatting in each device mode. (d) Force vs angle between the trunk and the hip characteristics of the device while stooping in each device mode.

to the length of the device in the minimum slack configuration for both test cases. We stretched the device by 100 mm and 167 mm in the two test cases, respectively, to account for the anticipated slack length of 67 mm.

Fig. 8(b) shows that when no patches are jammed with the origami muscle at its rest length, the device applies an assistive force with a stiffness of 0.58 N/mm (Mode 1). When the longer patch (Patch 1) is jammed, the device becomes stiffer, applying a force at 0.92 N/mm (Mode 2). With both the patches jammed, the device can apply a force at 1.7 N/mm (Mode 3). The designed stiffness values were 0.6 N/mm, 0.94 N/mm and 1.64 N/mm with $k_{\text{conn}} = 4.1$ N/mm computed inversely using (8). The root mean squared error (RMSE) in the experimental force compared to the analytical force was 3.88 N, 6.22 N, and 8.27 N in the low, medium, and high stiffness levels, respectively, potentially validating our model. Furthermore, existing soft, passive devices use a fixed stiffness of 0.8 N/mm [16], while our soft hybrid device offers three stiffness levels around this value. When the origami muscle is contracted, the slack in the device is reduced to zero, indicating that the device begins applying an assistive force as soon as the displacement occurs. The darker curves corresponding to the three stiffness levels with the contracted origami muscle are parallel to those representing the stiffness levels with the origami muscle at rest length. Further, the device provides a slack range from 0 to 67 mm that corresponds to a contraction ratio of 42.67% of the origami muscle.

V. Human Experiment

We conducted human experiments approved by the Institute Review Board at Arizona State University (STUDY0020698).

A. Experimental Protocol

The trunk angle α, defined as the sagittal plane angle between the torso and thigh was measured in human subjects using an 8-camera Vicon motion capture system (Vicon Motion Systems Ltd., Oxford, U.K.) and calculated with the Plug-in Gait marker set by summing the relative thorax and hip angles relative to the absolute pelvis angle [29]. A load cell (Model LCM300, FUTEK, accuracy $\pm 0.25\%$) was incorporated between the posture corrector and the upper muscle mount to measure the force applied by the device during the human experiment. All data were processed in MATLAB 2024a (MathWorks, Inc.), with kinematic data filtered using a fourth-order zero-lag 6 Hz low-pass filter, while raw load cell data was used without filtering.

Three subjects attended the lab on two separate days, including a squat and stoop lifting day, respectively. On each day, six randomized device modes were tested. After a detailed explanation of the protocol, subjects donned the device, after which the origami muscle was fully contracted, and the thigh straps were tightened to eliminate slack, ensuring maximum contraction corresponded to zero slack and the rest length provided 67 mm of slack. Before experiments, subjects completed a 30-second motion capture calibration trial. A 60 bpm metronome ensured a consistent 10-second squatting/stooping period.

B. Results and Discussion

Fig. 8(c) and (d) show the force measured by the load cell vs the the angle between the trunk and the hip across the six device modes during squatting and stooping, respectively. The force profiles during both squatting and stooping exhibit similar trends to those observed in the tensile testing. Quantitatively comparing the tensile test with the human experiments is challenging due to the non-linear and subject-specific relationship between the device stretch and trunk flexion angle. The non-zero load cell reading in the maximum slack modes (modes 1, 2, and 3) can be attributed to the partial device weight. With the 67 mm slack tuning, the device provides an angular slack range from 0 to 40° of trunk flexion. Due to the attachment and coupling with the human body, the peak forces in the human experiments were lower than those in the tensile testing. The aim of this work was to introduce and validate the tuning principles; we did not optimize the body attachments to achieve higher peak forces and instead used off-the-shelf attachments. Though the tuning is limited to linear force profiles, it has the potential to provide assistance closer to optimal value across a wider range of back movements than soft, passive devices without adding heavy and bulky parts like active devices.

The mode switching can be automated in the future with a thorough evaluation of the accuracy, robustness, and latency of the mode switching. While the origami muscle actuation is too slow for use during movement, slack adjustments can be completed beforehand, like increasing slack before sitting or walking.

VI. Conclusion

We proposed a lightweight, compact, soft BSD that offers assistive force profile tuning with three different stiffness levels and tunable slack. Our device improves upon state-of-the-art soft passive BSDs by enabling users to select a force profile without making it bulky and heavy like highly tunable active devices. We also presented an analytical model that facilitates the design of desired force profiles and validated the tuning capabilities of the device via human experiments.

Although we demonstrated force profile tuning on human subjects, future work should focus on optimizing the body attachment design to achieve a higher peak assistive force. Further investigation into the effects of device tuning on back muscle activity could provide valuable insights into the biomechanical benefits of the device's adjustable features. We envision that devices utilizing this tuning principle will be widely used in daily life, particularly for elderly individuals with weakened back muscles.

References

[1] S. A. Ferguson et al., "Prevalence of low back pain, seeking medical care, and lost time due to low back pain among manual material handling workers in the United States," *BMC Musculoskelet. Disord.*, vol. 20, no. 1, May 2019, Art. no. 243.

[2] J. Lo, L. Chan, and S. Flynn, "A systematic review of the incidence, prevalence, costs, and activity and work limitations of amputation, osteoarthritis, rheumatoid arthritis, back pain, multiple sclerosis, spinal cord injury, stroke, and traumatic brain injury in the United States: A 2019 update," *Arch. Phys. Med. Rehabil.*, vol. 102, no. 1, pp. 115–131, Jan. 2021.

[3] T. Kermavnar, A. W. de Vries, M. P. de Looze, and L. W. O'Sullivan, "Effects of industrial back-support exoskeletons on body loading and user experience: An updated systematic review," *Ergonomics*, vol. 64, no. 6, pp. 685–711, Jun. 2021.

[4] U. Granacher, A. Gollhofer, T. Hortobágyi, R. W. Kressig, and T. Muehlbauer, "The importance of trunk muscle strength for balance, functional performance, and fall prevention in seniors: A systematic review," *Sports Med.*, vol. 43, no. 7, pp. 627–641, Jul. 2013.

[5] R. Govaerts et al., "Evaluating cognitive and physical work performance: A comparative study of an active and passive industrial back-support exoskeleton," *Wearable Technol.*, vol. 4, Jan. 2023, Art. no. e27.

[6] K. Tsuneyasu, A. Ohno, Y. Fukuda, K. Ogawa, T. Tsuji, and Y. Kurita, "A soft exoskeleton suit to reduce muscle fatigue with pneumatic artificial muscles," in *Proc. 9th Augmented Hum. Int. Conf.*, New York, NY, USA: ACM, 2018, pp. 1–4.

[7] K. Zhu et al., "A smart, textile-driven, soft exosuit for spinal assistance," *Sensors*, vol. 23, no. 19, Jan. 2023, Art. no. 8329.

[8] M. Ide, T. Hashimoto, K. Matsumoto, and H. Kobayashi, "Evaluation of the power assist effect of muscle suit for lower back support," *IEEE Access*, vol. 9, pp. 3249–3260, 2021.

[9] A. S. Koopman, I. Kingma, M. P. de Looze, and J. H. van Dieën, "Effects of a passive back exoskeleton on the mechanical loading of the low-back during symmetric lifting," *J. Biomech.*, vol. 102, Mar. 2020, Art. no. 109486.

[10] S. Madinei, M. M. Alemi, S. Kim, D. Srinivasan, and M. A. Nussbaum, "Biomechanical evaluation of passive back-support exoskeletons in a precision manual assembly task: 'Expected' effects on trunk muscle activity, perceived exertion, and task performance," *Hum. Factors*, vol. 62, no. 3, pp. 441–457, May 2020.

[11] T. Poliero et al., "Versatile and non-versatile occupational back-support exoskeletons: A comparison in laboratory and field studies," *Wearable Technol.*, vol. 2, Jan. 2021, Art. no. e12.

[12] S. Kim, S. Madinei, M. M. Alemi, D. Srinivasan, and M. A. Nussbaum, "Assessing the potential for "undesired" effects of passive back-support exoskeleton use during a simulated manual assembly task: Muscle activity, posture, balance, discomfort, and usability," *Appl. Ergonom.*, vol. 89, Nov. 2020, Art. no. 103194.

[13] "FLEX Laevo," 2024. [Online]. Available: https://www.laevo-exoskeletons.com/en/flex

[14] J. Chung et al., "Lightweight active back exosuit reduces muscular effort during an hour-long order picking task," *Commun. Eng.*, vol. 3, no. 1, pp. 1–11, Feb. 2024.

[15] E. P. Lamers and K. E. Zelik, "Design, modeling, and demonstration of a new dual-mode back-assist exosuit with extension mechanism," *Wearable Technol.*, vol. 2, Jan. 2021, Art. no. e1.

[16] E. P. Lamers, A. J. Yang, and K. E. Zelik, "Feasibility of a biomechanically-assistive garment to reduce low back loading during leaning and lifting," *IEEE Trans. Biomed. Eng.*, vol. 65, no. 8, pp. 1674–1680, Aug. 2018.

[17] E. P. Lamers, J. C. Soltys, K. L. Scherpereel, A. J. Yang, and K. E. Zelik, "Low-profile elastic exosuit reduces back muscle fatigue," *Sci. Rep.*, vol. 10, no. 1, Sep. 2020, Art. no. 15958.

[18] S. M. Siedl, M. Wolf, and M. Mara, "Exoskeletons in the supermarket: Influences of comfort, strain relief and task-technology fit on retail workers' post-trial intention to use," in *Proc. Companion ACM/IEEE Int. Conf. Hum.-Robot Interact.*, New York, NY, USA, 2021, pp. 397–401.

[19] J. Babič et al., "Challenges and solutions for application and wider adoption of wearable robots," *Wearable Technol.*, vol. 2, Jan. 2021, Art. no. e14.

[20] M. Schwartz, J. Theurel, and K. Desbrosses, "Effectiveness of soft versus rigid back-support exoskeletons during a lifting task," *Int. J. Environ. Res. Public Health*, vol. 18, no. 15, Jan. 2021, Art. no. 8062.

[21] D. Schwerha, N. McNamara, S. Kim, and M. A. Nussbaum, "Exploratory field testing of passive exoskeletons in several manufacturing environments: Perceived usability and user acceptance," *IISE Trans. Occup. Ergonom. Hum. Factors*, vol. 10, no. 2, pp. 71–82, Aug. 2022.

[22] A. Di Lallo, S. Yu, J. E. Slightam, G. X. Gu, J. Yin, and H. Su, "Untethered fluidic engine for high-force soft wearable robots," *Adv. Intell. Syst.*, vol. 6, no. 11, 2024, Art. no. 2400171.

[23] Y. Roh, D. Lim, M. Kang, J. Cho, S. Han, and S. H. Ko, "Rigidity-tunable materials for soft engineering systems," *Adv. Eng. Mater.*, vol. 26, no. 13, 2024, Art. no. 2400563.

[24] B. Bazrgari, A. Shirazi-Adl, and N. Arjmand, "Analysis of squat and stoop dynamic liftings: Muscle forces and internal spinal loads," *Eur. Spine J.*, vol. 16, no. 5, pp. 687–699, May 2007.

[25] S. G. Fitzgerald, G. W. Delaney, and D. Howard, "A review of jamming actuation in soft robotics," *Actuators*, vol. 9, no. 4, Dec. 2020, Art. no. 104.

[26] B. Yang et al., "Reprogrammable soft actuation and shape-shifting via tensile jamming," *Sci. Adv.*, vol. 7, no. 40, 2021, Art. no. eabh2073.

[27] A. Sadeghi, A. Mondini, M. Totaro, B. Mazzolai, and L. Beccai, "A wearable sensory textile-based clutch with high blocking force," *Adv. Eng. Mater.*, vol. 21, no. 11, 2019, Art. no. 1900886.

[28] S. Li, D. M. Vogt, D. Rus, and R. J. Wood, "Fluid-driven origami-inspired artificial muscles," *Proc. Nat. Acad. Sci.*, vol. 114, no. 50, pp. 13132–13137, 2017.

[29] V. Nexus, "Full body modeling with Plug-in Gait - Nexus 2.16 documentation - Vicon Help," 2024. [Online]. Available: https://help.vicon.com/space/Nexus216/11607226/Full+body+modeling+with+Plug-in+Gait#Marker-placement-for-Plug-in-Gait-full-body-model